

Toward Suppressing Hydrogen Evolution with Enhanced Performance for Bi-Modified NaTi₂(PO₄)₃ Anodes in Aqueous Na-Ion Batteries

Fengting Cao,^[a] Xiaolong Shan,^[a] Jiangtao Wu,^[b, c] Yongxin Chen,^[b, d] Yang Zhou,^[b] Wenjun Wang,^{*[b]} and Chaoliu Zeng^{*[b]}

Aqueous sodium-ion batteries (ASIBs) show enormous difficulty to develop appropriate anode materials for their commercialization, mainly owing to the easy occurrence of hydrogen evolution from the decomposition of water at a negative potential with overlapping the operating potential of the anode for the Na⁺ intercalation/extraction reaction. Here, new anode materials Na_{1+x}Bi_xTi_{2-x}(PO₄)₃/C ($x=0, 0.005, 0.01, 0.02$) composites are prepared through introducing Bi elements into NaTi₂(PO₄)₃ (NTP, a promising anode material for ASIBs) with a facile sol-gel method. Thus, it firstly reports that the Bi doping can contribute to the inhibition of hydrogen evolution via regulation the electrode potential for hydrogen evolution at the

anode, also accompanying with excellent electrochemical and charge/discharge performances. The full cell constructed by Na_{0.44}MnO₂ as cathode and Bi-modified NTP as anode, exhibits the better cycling performance with a larger capacity retention of about 80.1% at 2 C-rate for 800 cycles and 80.2% at 10 C-rate for 1400 cycles in contrast with the pristine one (71.2%, 56.2%), respectively. Furthermore, the expansion of the charge cut-off voltage resulted from the inhibition of hydrogen evolution after Bi doping into NTP can finally increase the discharge capacity and energy density of the modified full cell by 21.8% and 17.3%, respectively.

1. Introduction

In recent years, with the rapid development of modern portable electronic products, new energy vehicles, and grid energy storage technology, the demand for advanced battery energy storage systems has greatly increased.^[1–3] Sodium ion batteries (SIBs) have gained widespread attention due to their abundant reserves and low cost, and show enormous potential in large-scale renewable energy storage.^[4–8] Therefore, the development of high energy density, stable, and sustainable sodium ion battery materials still requires a lot of research work.

Organic SIBs utilize toxic, flammable, and volatile organic electrolytes, facing environmental challenges and safety risks.^[9,10] Aqueous batteries use water-based electrolytes, which have advantages such as cost-effectiveness, safety, high power density, and scalable energy storage.^[11–13] In the field of commercial aqueous batteries, the main challenges include

limited electrochemical stability window of water, limited charge storage capacity and poor cycling stability of electrode materials.^[14,15] Therefore, there is an urgent need to promote the development of electrochemical active materials with high discharge capacity and long cycle life in aqueous electrolytes, as this is crucial for the successful commercialization of aqueous sodium ion batteries (ASIBs). Different electrode materials for SIBs have been explored in recent years, including transition metal layered oxides,^[1] Prussian blue analogues,^[16] and poly-anionic compounds.^[17,18] Among them, phosphate-based poly-anionic compounds are fairly optimal as negative electrode materials due to their stability, safety, low cost, and structural diversity.^[19] Due to its structural stability and diversity, phosphate framework materials are not only typical solid ion conductors,^[20] but also low-cost electrode materials that are very suitable for other devices such as sodium ion batteries and lithium ion batteries.^[21,22]

Among these phosphate-based compounds, the sodium (Na) superionic conductor (NASICON)-type structure is considered to provide a highly conductive pathway for Na⁺ migration, thus possessing strong sodium storage performance.^[23] Among the NASICON-type compounds, sodium titanium phosphate (NaTi₂(PO₄)₃, NTP) has received increasing attention due to its high theoretical capacity of 133 mAh g⁻¹, low cost, good safety, high structural stability, open channels, and flat charge/discharge plateaus.^[24–28] It is recognized as one of the most promising negative electrode materials in ASIBs. However, the NASICON structure also places restrictions on the electrical conductivity of NTP.^[29] Moreover, some studies have reported that the NTP material commonly tends to lose function over tens or several hundred cycles, especially when cycled deeply

[a] F. Cao, X. Shan

School of Mechanical Engineering, Tianjin Key Laboratory of High Performance Manufacturing Technology & Equipment, Tianjin University of Technology and Education, Tianjin 300222, P. R. China

[b] J. Wu, Y. Chen, Y. Zhou, W. Wang, C. Zeng

Songshan Lake Materials Laboratory, Dongguan 523808, P. R. China
E-mail: wangwenjun@sslab.org.cn
zengchaoliu@sslab.org.cn

[c] J. Wu

Institute of Metal Research, Chinese Academy of Sciences, Shenyang 110016, P. R. China

[d] Y. Chen

School of Chemistry, South China Normal University, Guangzhou 510006, P. R. China

or slowly at low C-rates less than 1 C, leading to the inferior cycling stability of the NTP anode.^[30,31] The poor cycling stability of NTP is mainly attributed by the possible dissolution of NTP active materials in aqueous electrolytes and the hydrogen evolution from the decomposition of water.^[32,33] Thus, some effective modifications of NTP including ion doping^[29,34] and coating NTP with conductive materials^[35–38] have been proposed to promote the electrical conductivity and cycling stability of NTP.

On one hand, the doping of impurity atoms into NTP, especially partially or fully replacing Ti element in NTP with elements such as Mn,^[39] Mg,^[40] V,^[41] Fe,^[42,43] can improve its ionic conductivity, structural stability, and electrochemical performance to some extent, thereby promoting its discharge capacity and cycling stability. The authors also prepared NASICON-structured $\text{Na}_{1.1}\text{Al}_{0.1}\text{Ti}_{1.9}(\text{PO}_4)_3/\text{C}$ ^[29] and $\text{Na}_{3.4}\text{Mn}_{1.2}\text{Ti}_{0.8}(\text{PO}_4)_3/\text{C}$ ^[44] composites, applied as the promising anode and cathode materials in ASIBs, respectively. On the other hand, coating NTP with conductive carbon materials,^[35,36] polypyrrole (PPY) conductive polymers^[38] and TiN^[37] have been recently obtained to hinder the direct contact between the NTP anode and the aqueous electrolyte, and thus suppress the possible dissolution of NTP active materials in aqueous electrolytes, accompanying with the improvement of the electrical conductivity and cycling stability of NTP. An artificial poly-pyrrole protective interphase layer was also constructed by the authors for the NTP anode to suppress the unwanted side reactions at the electrode/electrolyte interface, and obtained some desired results.^[38] Although a variety of methods have been used to promote the electrical conductivity and cycling stability of NTP, it should still be noted that the key obstacle that prevents the popularization of NTP in ASIBs is the inadequate operating potential (-0.581 V vs. NHE) for the Na^+ intercalation/extraction reaction, which is too close to the hydrogen evolution potential (-0.591 V vs. NHE).^[42] Then, during the NTP charging process, a potential overlap between sodiation and H_2O reductive decomposition might come out easily, accompanying with the occurrence of hydrogen evolution at the NTP anode, even if the electrode polarization potentials contributed by the kinetic factors in the reaction process are considered. Furthermore, the above-mentioned irreversible hydrogen evolution reaction might increase the internal pressure of the battery and deplete the limited Na^+ in the cathode material, thus decreasing the battery safety and capacity with a rapid deterioration.^[42] Therefore, increasing the operating potential of NTP and decreasing the hydrogen evolution potential are very important technical keys to suppress hydrogen evolution for commercializing NTP in ASIBs.

Recently, Qiu et al^[42] have firstly reported a redox potential regulation strategy to overcome this technical problem by integrating the redox couples of $\text{Ti}^{4+}/\text{Ti}^{3+}$ and $\text{Fe}^{3+}/\text{Fe}^{2+}$ to yield $\text{Na}_{1.5}\text{Ti}_{1.5}\text{Fe}_{0.5}(\text{PO}_4)_3$ (NTFP) and increasing its operating potential up to -0.498 V vs. NHE, which effectively prevents the potential overlap with the reductive decomposition of H_2O . However, it is worth noting that increasing the operating potential of the NTP anode for the Na^+ intercalation/extraction process can inhibit the occurrence of hydrogen evolution, however, with the decreasing operating potential of the full cell

during discharging, thereby reducing the discharge capacity and energy density of the full cell. Furthermore, if the inhibition of hydrogen evolution at the negative side was resulted from the decreasing potential for hydrogen evolution at the anode, rather than the increasing operating potential of NTP, the NTP anode could actually operate at a lower potential during the charge/discharge process. Thus, it could ensure that the full cell has a higher operating potential during discharge, thereby improving the discharge energy density, cycle life, and coulombic efficiency of the battery. Based on the above analysis, it is of great necessity to produce new anode materials for ASIBs to suppress the occurrence of hydrogen evolution via decreasing the potential for hydrogen evolution at the negative side.

In this study, we prepared new anode materials $\text{Na}_{1+x}\text{Bi}_{x}\text{Ti}_{2-x}(\text{PO}_4)_3/\text{C}$ ($x=0, 0.005, 0.01, 0.02$) composites through introducing Bi elements into NTP with a facile sol-gel method, and it firstly reports that the Bi doping can contribute to the inhibition of hydrogen evolution via regulation the electrode potential for hydrogen evolution at the NTP anode, also accompanying with excellent electrochemical and charge/discharge performances. Furthermore, the excellent stability and high efficiency of the aqueous half-cells and full-cells with long-term cycling suggests the importance of inhibiting electrolyte decomposition to maintain the Na^+ reversible activity in the full-cells.

Experimental

Materials Synthesis

The $\text{Na}_{1+x}\text{Bi}_{x}\text{Ti}_{2-x}(\text{PO}_4)_3/\text{C}$ composites as anode were prepared by a facile sol-gel method, as reported in our previous work.^[29,38] Firstly, Na_2CO_3 , $\text{NH}_4\text{H}_2\text{PO}_4$ and certain amounts of citric acid was mixed and solved in deionized water. And then, tetrabutyl titanate diluted by ethanol was added into the above-mentioned mixed solution with stirring on the electro-thermostatic water bath. After evaporation of the solvent, the precursor was sintered at 350°C for 4 h and then 800°C for 10 h under argon atmosphere to obtain the undoped $\text{NaTi}_2(\text{PO}_4)_3/\text{C}$ products. Then, the three Bi doped samples were synthesized in the same way, except that stoichiometric $\text{Bi}(\text{NO}_3)_3$ was added in the deionized water before the addition of tetrabutyl titanate diluted by ethanol. And the amount of Na_2CO_3 and tetrabutyl titanate should be adjusted based on the stoichiometric ratio of the target doped products. The obtained $\text{Na}_{1+x}\text{Bi}_{x}\text{Ti}_{2-x}(\text{PO}_4)_3/\text{C}$ ($x=0, 0.005, 0.01, 0.02$) were denoted as NTP, NBTP-0.005, NBTP-0.01, and NBTP-0.02, respectively. It should be also noted that too much Bi doped with the value of x higher than 0.05, will easily result in the occurrence of certain impurities in the obtained samples except for the NTP/C main phase. Additionally, $\text{Na}_{0.44}\text{MnO}_2$ as cathode was produced with MnCO_3 and Na_2CO_3 as starting materials by solid-state reaction, as similarly reported in the previous work,^[45] and the corresponding process parameter optimization have been shown in detail in another unpublished paper submitted.

Materials Characterization

The crystal structure and phase component of the as-synthesized samples were identified by powder X-ray diffraction (XRD, Panalytical

X'Pert-Pro) using the $K\alpha$ radiation ($\lambda = 0.154$ nm) in the range of 2θ from 10° to 90° . Raman spectroscopy (Raman, Horiba LabRam HR Evolution) was performed to confirm the presence of carbon materials in the obtained samples. The surface morphology of the samples was observed by using scanning electron microscopy (SEM, Zeiss Gemini 300) and transmission electron microscopy (TEM, JEOL JEM-F200). X-ray photoelectron spectroscopy (XPS, Thermo Fisher ESCALAB XI+) was performed to examine the elemental composition and valence state of samples, with XPS Peak 4.1 employed to deconvolve the Ti2p and Bi4f peaks.

Electrochemical Measurements

The electrochemical performances of the anodes in 1.0 M Na_2SO_4 aqueous electrolytes were examined with a conventional three-electrode cell using a platinum foil as the counter electrode and a saturated calomel electrode (SCE, 0.244 V) as the reference electrode. A salt bridge was applied to decrease the liquid junction potential between the Luggin capillary and the working electrode. The working electrode is composed of active material, carbon black, and polytetrafluoroethylene (PTFE), with a mass ratio of 7:2:1. Briefly, active materials and carbon black were mixed under constant grinding in an agate mortar. Then PTFE was added to the mixture to form the electrode paste. The working electrode was obtained by pressing the paste onto a Ti mesh (100 mesh) current collector. The typical mass loading and thickness of the active material in the anode was approximately $6\text{--}7\text{ mg cm}^{-2}$ and $50\text{ }\mu\text{m}$, respectively. Cyclic voltammograms (CV) and potentiodynamic polarization curves were obtained with a Gamry 1000E Electrochemical Analysis Instrument. The galvanostatic charge/discharge measurements for the as-prepared anodes with the above-mentioned three-electrode cell were carried out on a Land CT2001A battery test system (Wuhan, China). The charge/discharge capacities were estimated in units of mAh g^{-1} based on the mass of the NTP/C active materials of the anodes and the rates in the C-rate convention whereas 1 C corresponds to 133 mA g^{-1} . Unless otherwise indicated, all potentials reported in this work were referred to SCE.

In addition, a CR2025 coin cell configuration was employed to examine the electrochemical performance of the full cell with NMO as cathode and Bi-doped NTP/C as anode. The full cell applied glass fiber as the separator and 1.0 M Na_2SO_4 as the aqueous electrolyte, respectively. The anode contains $6\text{--}7\text{ mg cm}^{-2}$ active materials with thickness of $50\text{ }\mu\text{m}$, while the cathode has $12\text{--}13\text{ mg cm}^{-2}$ NMO with thickness of $350\text{ }\mu\text{m}$. Accordingly, the capacity ratio of the cathode and anode was about 1.2:1, which ensured an anode-limited full cell. Cyclic voltammetry (CV) and Galvanostatic charge/discharge tests were also conducted for the full cells. The specific capacity and specific energy density of the full cell with NMO as cathode and Bi-doped NTP/C as anode were also estimated based on the mass of active material in the anode.

2. Results and Discussion

The crystal structure and chemical composition of the as-synthesized samples in this work were identified by the X-ray diffraction analysis. As shown in Figure 1a, all the diffraction peaks of the XRD patterns for the obtained products can be fully indexed based on the predicted JCPDS pattern of $NaTi_2(PO_4)_3$ with rhombohedral R-3c space group. It can be also observed that no impurity was detected in the patterns of the obtained samples, indicating that an appropriate proportion of

Bi doping has little affect the crystal structure of $NaTi_2(PO_4)_3$. In addition, there are no carbon dispersion peaks observed from the XRD patterns of Figure 1a, suggesting that the carbon coating on the NTP surface exists in an amorphous form. It should be noted that the (113) diffraction peak gradually shifts to smaller angles with the increasing Bi doping content. It indicates that the unit cell volume has increased, possibly resulted from the larger ion radius of Bi^{3+} (1.03 Å) than that of Ti^{4+} (0.605 Å) introduced into the NTP crystal structure. Furthermore, the determined lattice cell parameters of the obtained phases in this work can be estimated by fitting with Jade 5.0, and then the cell volume can be also calculated, as illustrated in Table 1. Thus, the change of the lattice parameters and cell volume with the Bi doping content for the above samples was presented in Figures 1b and c. It can be seen that all the lattice parameters including the values of a , b and c almost increase when the value of x becomes larger, and the NTP unit cell volume increases from 1358.960 to 1361.497 Å³. It can be concluded that Bi^{3+} is successfully doped into the NTP lattice. The increase in the unit cell volume indicates a larger transport channel for Na^+ ions in the NTP crystal structure, thus promoting the electrochemical kinetics. Also, it can be concluded that Bi^{3+} is successfully doped into the NTP lattice. As reported in the previous work,^[46] an ingenious strategy of Bi^{3+} (1.03 Å) substitution at V^{3+} (0.74 Å) site in $Na_3V_2(PO_4)_3$ (NVP) was also similarly proposed for developing the cathode in organic sodium ion batteries. The introduction of Bi into NVP can further expand the crystal structure inside the NVP, thus accelerating the migration of Na^+ , and the obtained structural framework of $Na_3V_{2-x}Bi_x(PO_4)_3/C$ also shows that the $(Bi_xV_{2-x}O_6)$ octahedra and (PO_4) tetrahedra are co-topically attached to the C-axis, forming a larger gap of the polyanion unit for Na^+ migration.^[46] Owing to the similar ion radius and polyanion unit for the corresponding Ti^{4+} and V^{3+} ions, the obtained $Na_{1+x}Bi_xTi_{2-x}(PO_4)_3/C$ in this work might be thought to have a similar structural framework containing the $(Bi_xTi_{2-x}O_6)$ octahedra and (PO_4) tetrahedra with the above-mentioned $Na_3V_{2-x}Bi_x(PO_4)_3/C$, also forming a larger gap of the polyanion unit for Na^+ migration. Additionally, the carbon content of the above-mentioned composites can be estimated to be about 9% through the thermogravimetric (TG) analysis, as reported in our previous work.^[38]

To further confirm the presence of carbon, Figure 2 shows the Raman spectra of NTP, NBTP-0.005, NBTP-0.01, and NBTP-0.02. It can be observed that there are three obvious Raman characteristic peaks for all the above samples. The peak at 1354 cm^{-1} (D band) and the peak at 1600 cm^{-1} (G band)

Table 1. Cell Parameters in R-3 C Space Groups of NTP, NBTP-0.005, NBTP-0.01, and NBTP-0.02 Samples.

Samples	$a=b/\text{\AA}$	$c/\text{\AA}$	$V/\text{\AA}^3$
NTP	8.459	21.930	1358.960
NBTP-0.005	8.463	21.933	1360.325
NBTP-0.01	8.465	21.937	1361.205
NBTP-0.02	8.466	21.938	1361.497

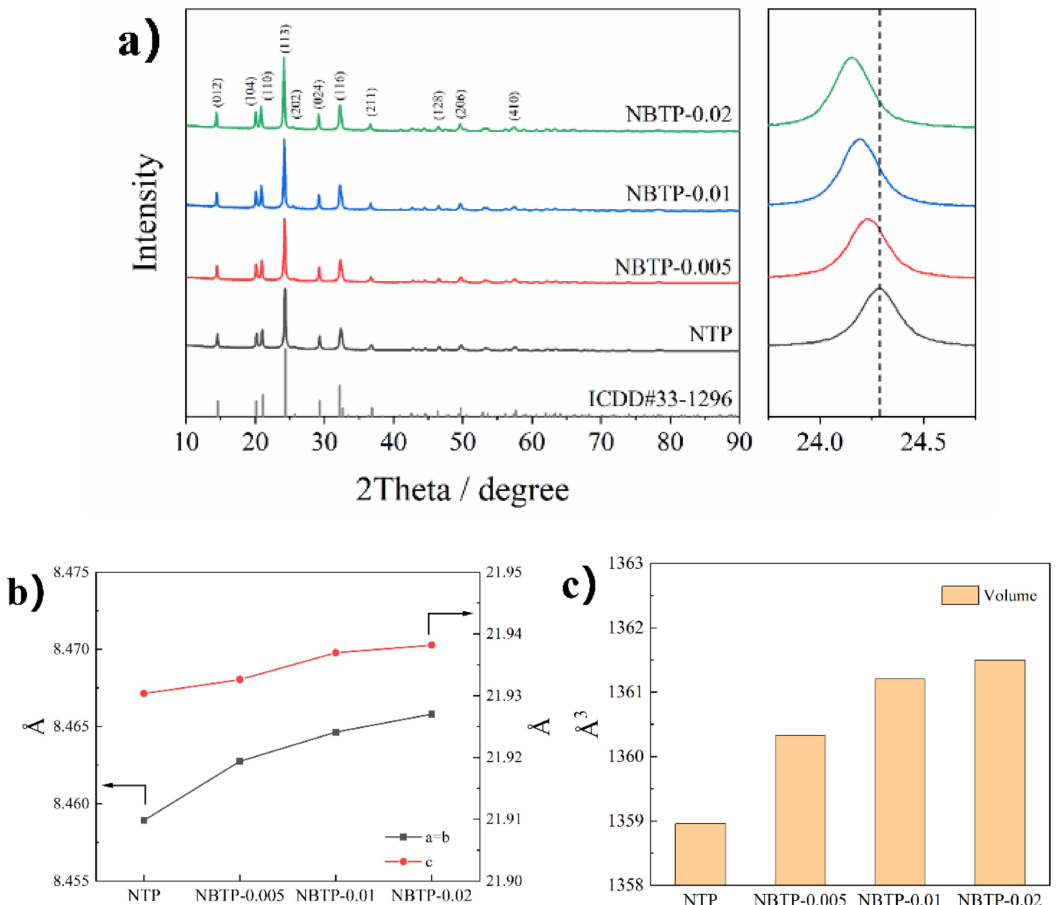


Figure 1. (a) XRD data from NTP, NBTP-0.005, NBTP-0.01 and NBTP-0.02 with JCPDS predicted pattern overlay; (b) The changes in lattice parameters for the as-prepared samples. (c) The changes in cell volume for the as-prepared samples.

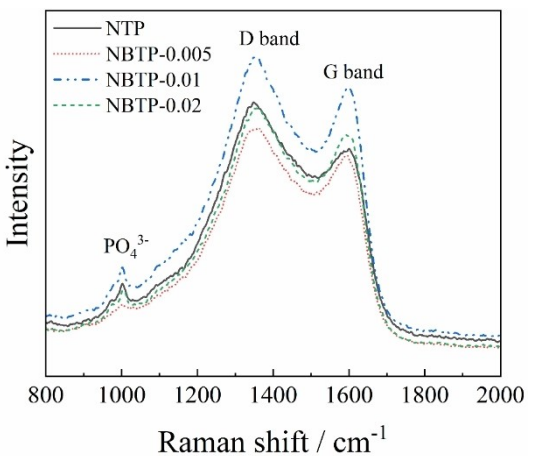


Figure 2. Raman spectra of NTP, NBTP-0.005, NBTP-0.01, and NBTP-0.02.

correspond to the amorphous carbon and the graphitic carbon, respectively. Moreover, the peak at 1001 cm^{-1} represents the stretching vibration of P–O bonds in phosphate tetrahedra, and the characteristic peak of PO_4^{3-} is rather weak.^[29] Furthermore, the intensity ratio of D band and G band (I_D/I_G) can be estimated to evaluate the degree of defect in carbon for the above

samples. Thus, the values of I_D/I_G of NTP, NBTP-0.005, NBTP-0.01, and NBTP-0.02 can be calculated to be 1.18, 1.11, 1.10, and 1.11, respectively, suggesting the amorphous nature of the carbon coatings in the above-mentioned four samples, which is consistent with the above-mentioned XRD results.

Figure 3 illustrates SEM images of NTP, NBTP-0.005, NBTP-0.01, and NBTP-0.02. In comparison with the NTP, the other three Bi-doped samples show the stronger agglomeration in the secondary microscale particles, possibly due to the formation of the smaller primary nanoparticles of NTP resulted from the Bi doping. Moreover, all the samples are composed of primary nanoparticles about 200–400 nm as presented in the inset of Figure 3c. As can be seen, the morphology of the four samples is composed of scattered irregular particles with sizes ranging from hundreds of nanometers to several microns. Thus, there is no significant difference in the particle morphology between the NTP and Bi-doped samples, suggesting that Bi doping has little effect on the morphology of NTP. In addition, the EDS elemental mapping of NBTP-0.01 is also displayed in Figure 3, indicating that Na, Bi, Ti and P elements are uniformly distributed in the sample. It can be also confirmed that the Bi element is successfully introduced into the NTP material.

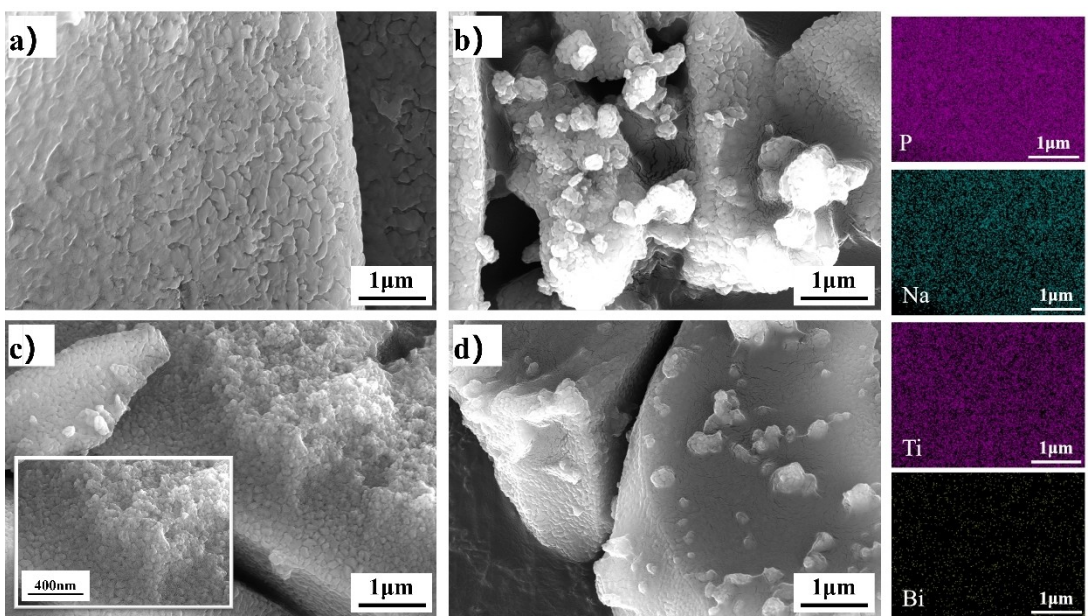
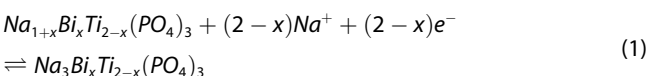


Figure 3. SEM images of NTP (a), NBTP-0.005 (b), NBTP-0.01 (c), and NBTP-0.02 (d), with the EDS elemental mapping of NBTP-0.01 included.

To further characterize the particle morphologies, Figure 4 gives TEM images of NTP and NBTP-0.01. The carbon layer with the thickness of about 5 nm can be observed to be compactly coated at the NTP particle for both the NTP and NBTP-0.01 samples, predominately owing to the high-temperature decomposition of citric acid in the precursors to ensure good electronic conductivity of the samples. Clear lattice stripes can be seen in Figures 4b and d, with interplanar spacing of 0.159 and 0.180 nm, corresponding to the (116) and (110) crystal plane of $\text{NaTi}_2(\text{PO}_4)_3$, respectively. It is also indicated that both the as-synthesized NTP and NBTP-0.01 show good crystallinity.

X-ray photoelectron spectroscopy (XPS) was conducted with the carbon (C 1s = 284 eV) applied to calibrate binding energies, in an attempt to confirm the elemental composition and valence state in NBTP-0.01, as shown in Figure 4. Figure 4e gives the XPS full spectrum of the NBTP-0.01, suggesting that the binding energies at 1073, 532, 460, 284, 163 and 133 eV correspond to Na 1s, O 1s, Ti 2p, C 1s, Bi 4f, and P 2p, respectively.^[29] It should be noted that the Bi 4f peak is rather low in the full spectra of Figure 4e, also indicating a low amount of Bi element introduced into the NTP lattice. Then, the high-resolution spectrum of Bi 4f was further detected, as shown in Figure 4f. It can be observed from Figure 4f that two distinct peaks are located at 164.9 and 159.6 eV corresponding to Bi^{3+} 4f_{5/2} and Bi^{3+} 4f_{7/2},^[46] indicating that Bi^{3+} is successfully introduced into the NTP lattice. Moreover, to have a better understanding of the variety of the valence states of Ti, Figure 4g shows the high-resolution spectrum of Ti 2p in the same sample. It shows that there are two diffraction peaks for the NBTP-0.01 sample at around 460.0 (Peak 1) and 465.8 eV (Peak 2) with respect to Ti^{4+} 2p_{3/2} and Ti^{4+} 2p_{1/2},^[29] which are well consistent with the Ti^{4+} ions in an octahedral environment of $\text{NaTi}_2(\text{PO}_4)_3$.

As shown in Figures 5–8, all the electrochemical and charge/discharge curves of the corresponding NTP, NBTP-0.005, NBTP-0.01 and NBTP-0.02 samples were examined with a conventional three-electrode cell using a platinum foil as the counter electrode and a saturated calomel electrode (SCE, 0.244 V) as the reference electrode. In order to investigate the electrochemical behavior among the NTP, NBTP-0.005, NBTP-0.01, and NBTP-0.02 anode materials, cyclic voltammetry (CV) was conducted to examine the electrochemical reaction activities at these four electrodes in 1.0 M Na_2SO_4 aqueous solution at a scan rate of 0.5 mVs⁻¹. As shown in Figure 5a, there are a pair of redox peaks for all the above samples at around -0.9 and -0.78 V, with respect to the $\text{Ti}^{4+}/\text{Ti}^{3+}$ redox reaction in $\text{Na}_{1+x}\text{Bi}_x\text{Ti}_{2-x}(\text{PO}_4)_3$, accompanying with the intercalation/extraction of Na^+ in the NTP lattice. The corresponding electrochemical reaction is as follows:



For the NBTP-0.005, NBTP-0.01 and NBTP-0.02 samples, the doped Bi^{3+} has the electrochemical inertness and does not participate in the electrochemical reactions. Bi doped-NTP, especially NBTP-0.01, has the higher peak current density in contrast with NTP. Moreover, the peak current density of NBTP-0.005 and NBTP-0.02 are also smaller than that of NBTP-0.01. The values of the separations between the oxidation and the reduction peak potentials (ΔE_p) for the NTP, NBTP-0.005, NBTP-0.01 and NBTP-0.02 anodes are estimated to be 126, 128, 124 and 140 mV, respectively. It suggests that the NBTP-0.01 anode has the highest reaction current, the smallest value of ΔE_p , and thus the best reaction activity among the four ones, also suggesting that $\text{NaTi}_2(\text{PO}_4)_3$ doped with an appropriate amount

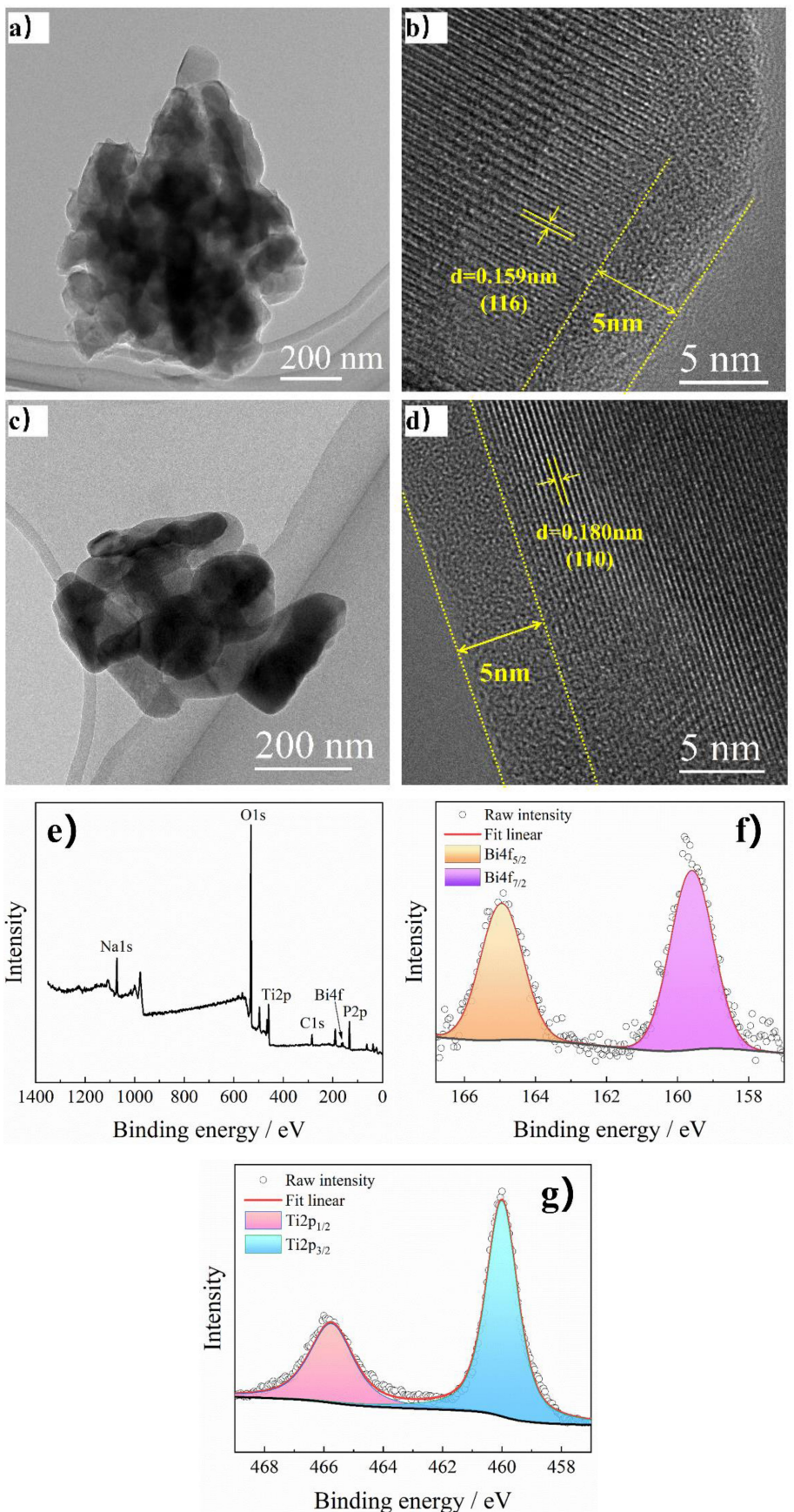


Figure 4. TEM images of NTP (a, b) and NBTP-0.01(c, d), (e) Full XPS spectrum of NBTP-0.01, (f) Bi 4f high-resolution XPS spectrum of NBTP-0.01, (g) Ti 2p high-resolution XPS spectrum of NBTP-0.01.

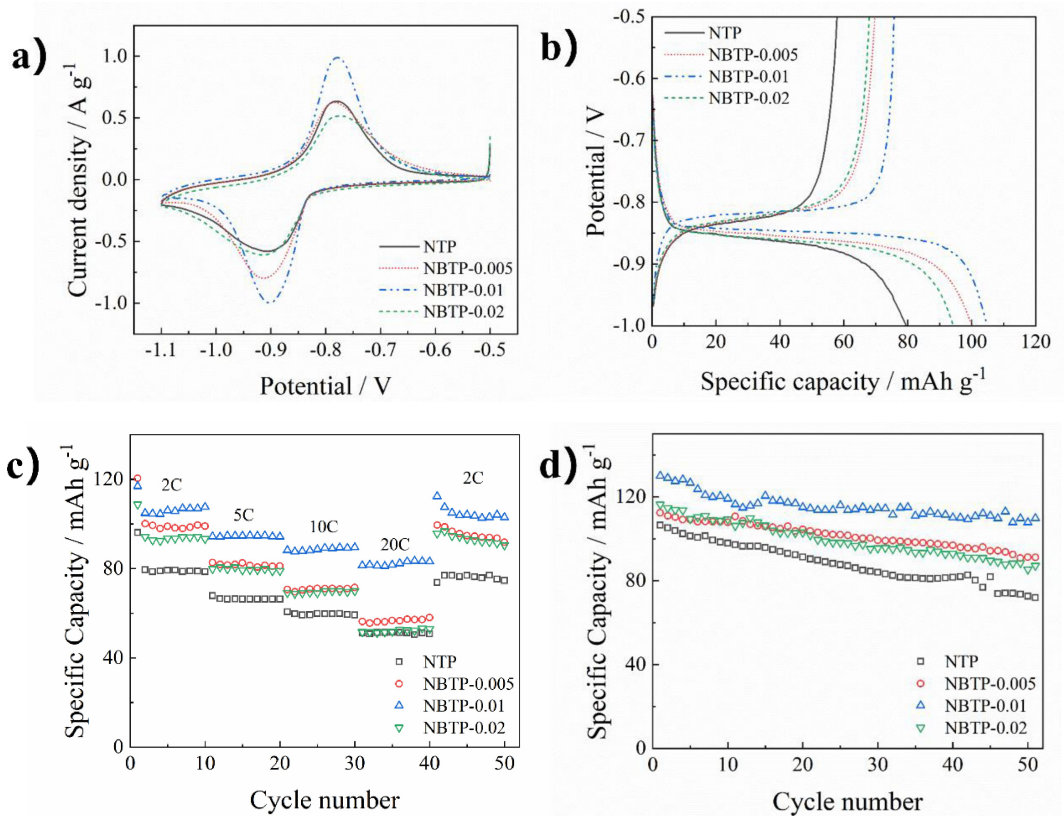


Figure 5. Electrochemical performance of NTP, NBTP-0.005, NBTP-0.01, and NBTP-0.02: (a) cyclic voltammetry curve; (b) charge discharge curve at 2 C; (c) rate performance; (d) cyclic performance at 1 C.

of bismuth has the better electrode reaction activity with respect to the Na^+ intercalation/extraction compared to the pristine sample. The better electrochemical kinetics resulted from the Bi doping is probably due to the larger transport channel for Na^+ ions in the Bi-modified NTP crystal structure in this work. However, it should be noted that the NBTP-0.01 has the best electrode activity, rather than the NBTP-0.02 with the more added Bi ($x=0.02$), might owing to the decrease in the theoretical capacity of $\text{Na}_{1+x}\text{Bi}_x\text{Ti}_{2-x}(\text{PO}_4)_3$ active materials with increasing the inactive bismuth.

Figure 5b shows the charge/discharge curves of the NTP, NBTP-0.005, NBTP-0.01 and NBTP-0.02 samples at a 2 C-rate. All the samples show a charge/discharge voltage plateau around -0.83 V (vs. SCE) with respect to the $\text{Ti}^{4+}/\text{Ti}^{3+}$ redox reaction in $\text{Na}_{1+x}\text{Bi}_x\text{Ti}_{2-x}(\text{PO}_4)_3$, which is consistent with the CV results in Figure 5a. It can be observed that the discharge capacity of the undoped NTP sample is 79.5 mAh g^{-1} . As the amount of the bismuth doping increases from 0 to 0.01, its discharge capacity gradually increases, with the value of 104.8 mAh g^{-1} for the NBTP-0.01 sample. However, further increasing the doping amount to be $x=0.02$, the discharge capacity of the NBTP-0.02 one decreases to be 94.2 mAh g^{-1} . This may be due to that the substitution of Ti with excessive electrochemically inert bismuth leads to a decrease in the theoretical capacity of the anode, which is consistent with the CV results in Figure 5a. Of course, the largest capacity value of 104.8 mAh g^{-1} for the NBTP-0.01 sample, more than that of 79.5 mAh g^{-1} for the pristine one, also

might be resulted from the larger transport channel for Na^+ ions with the Bi doping in this work.

Further tests were conducted on the rate and cycling performance of the above-mentioned four samples. Figure 5c presents the plots of the discharge capacities vs. cycle number for the NTP, NBTP-0.005, NBTP-0.01, and NBTP-0.02 at varying rates including 2, 5, 10, 20 C-rate, and back to 2 C-rate. NBTP-0.01 provides the discharge capacities of 104.8, 94.4, 88.6 and 81.7 mAh g^{-1} at 2, 5, 10 and 20 C rates, respectively, and retains a discharge capacity of 104.1 mAh g^{-1} with a high capacity retention of 99.3% when returning to 2 C-rate. The corresponding smaller values for the NTP sample are 79.6 (2 C), 66.3 (5 C), 59.7 (10 C), and 51.1 (20 C) and retains 76.5 mAh g^{-1} with a capacity retention of 96.1%, in comparison with the NBTP-0.01 sample. Therefore, it can be also observed from the plots of Figure 5c that the NBTP-0.01 has the best rate performance with the largest discharge capacity and the highest capacity retention at different C-rates among the four samples. Figure 5d shows the plots of discharge capacity as a function of cycle number for the NTP, NBTP-0.005, NBTP-0.01, and NBTP-0.02 samples at 1 C rate for 50 cycles. All samples show a certain degree of capacity decay during the cycling of the charge/discharge process, which may be caused by some side reactions at the electrode/electrolyte interface. The initial discharge capacity of NBTP-0.01 is 130.0 mAh g^{-1} , and after 50 cycles, the capacity is 109.8 mAh g^{-1} with a capacity retention of 84.5%. In contrast, NTP has an initial discharge capacity of 106.5 mAh g^{-1} ,

and after 50 cycles, the capacity is 71.9 mAh g^{-1} with a capacity retention rate of 67.5%. It is indicated that the NBTP-0.01 has the better cycling performance than that of the NTP. Thereby, the NBTP-0.01 has the best rate performance with the largest discharge capacity and the best cycling performance among the above-mentioned four samples. The above-mentioned previous work^[46] on the introduction of Bi into NVP to form $\text{Na}_3\text{V}_{2-x}\text{Bi}_x(\text{PO}_4)_3/\text{C}$, also reported that the introduction of bismuth ions slightly increases the cell size, while the solid BiO_6 serve as a stable and larger diffusion channel for the migration of Na^+ within the NVP structure, thus exhibiting a longer cycle life and higher rate performance for the modified composites in comparison with the pristine one. Consequently, the best rate performance and cycling performance for the modified NBTP-0.01 composite also might be due to the possible formed solid BiO_6 octahedra served as a stable and larger diffusion channel for the migration of Na^+ within the NTP structure in this work.

Furthermore, the reaction kinetics of NTP and NBTP-0.01 at various scanning rates were examined using the CV method, as seen in Figures 6a and b. As shown in Figure 6c, the plots of I_p vs. $v^{1/2}$ can be obtained from the CV curves of Figures 6a and b. It illustrates that there is a linear relationship between the peak current (I_p) and the square root of the scan rate ($v^{1/2}$), indicating that the electrochemical reactions for the NTP and NBTP-0.01

samples are the typical diffusion-controlled processes. The Randles- Sevcik equation can be shown as follows:^[29]

$$I_p = 0.4463n^{3/2}F^{3/2}R^{-1/2}T^{-1/2}ACD^{1/2}v^{1/2} \quad (2)$$

In the equation, I_p is the peak current of the cathode or anode, n is the number of electrons per molecule during embedding, F is Faraday constant, R is gas constant, T is absolute temperature, A is the effective contact area between the electrode and electrolyte, C is the concentration of Na^+ in the electrode, D is the diffusion coefficient of Na^+ , and v is the scan rate. According to Equation (2), the diffusion coefficients of the anode and cathode processes of NTP can be calculated to be 1.65×10^{-8} and $1.37 \times 10^{-8} \text{ cm}^2 \text{s}^{-1}$, respectively. The corresponding diffusion coefficients of NBTP-0.01 are 6.72×10^{-8} and $6.58 \times 10^{-8} \text{ cm}^2 \text{s}^{-1}$, respectively. It suggests that the diffusion coefficients of Na^+ for the NBTP-0.01 anode are higher than those for the NTP anode. It is also confirmed that the larger transport channel for Na^+ ions in the crystal structure by the Bi doping can evidently accelerate the ion diffusion of Na^+ and improve the intrinsic ion conductivity of the Bi-modified system, thus promoting the electrochemical kinetics and the charge/discharge capacities.

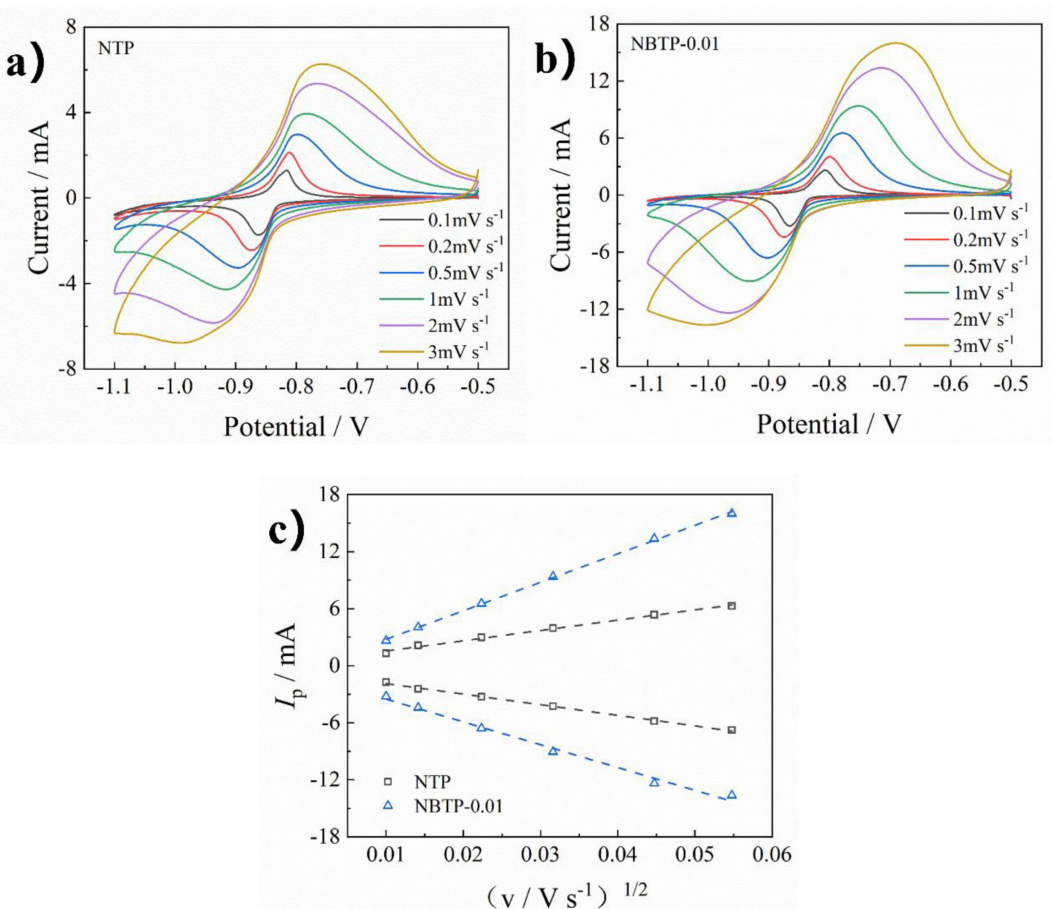


Figure 6. Cyclic voltammograms of NTP (a) and NBTP-0.01 (b) at various scan rates, and the relationship between peak current (I_p) and the square root of scan rate ($v^{1/2}$).

Figure 7 shows the long-term cycling performance of the NTP, NBTP-0.005, NBTP-0.01, and NBTP-0.02 half-cells at a 10 C-rate. The NTP, NBTP-0.005, NBTP-0.01 and NBTP-0.02 half-cells deliver the initial discharge capacities of 61.4, 72.0, 87.7 and 70.6 mAh g⁻¹ after 200 cycles, with the corresponding capacity retention of 77.5%, 78.5%, 79.2% and 75.5%, respectively. Thereby, it can be obtained that the NBTP-0.01 half-cell has the highest capacity retention and thus the best cycling performance among the four samples. It further suggests that the

appropriate amount of Bi doping is greatly beneficial to enhance the long-term cycling performance of the above-mentioned system, also owing to that the possible formed solid BiO₆ octahedra serves as a stable and larger diffusion channel for the migration of Na⁺ within the NTP structure by the Bi doping.^[46]

The hydrogen evolution phenomenon that easily occurs at the anode potential is a huge obstacle for the application of anode materials in ASIBs. Figure 8a gives the linear voltammetry

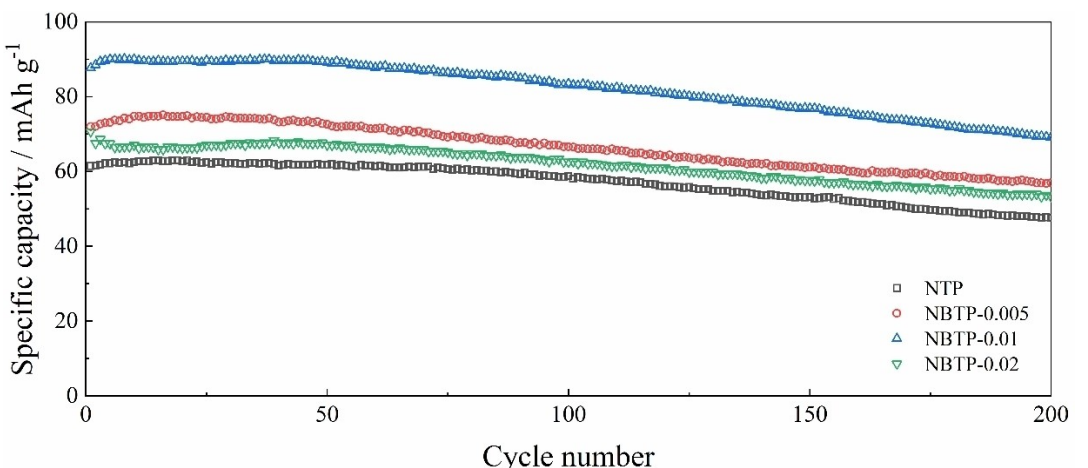


Figure 7. Cycle performance of NTP, NBTP-0.005, NBTP-0.01, and NBTP-0.02 at 10 C

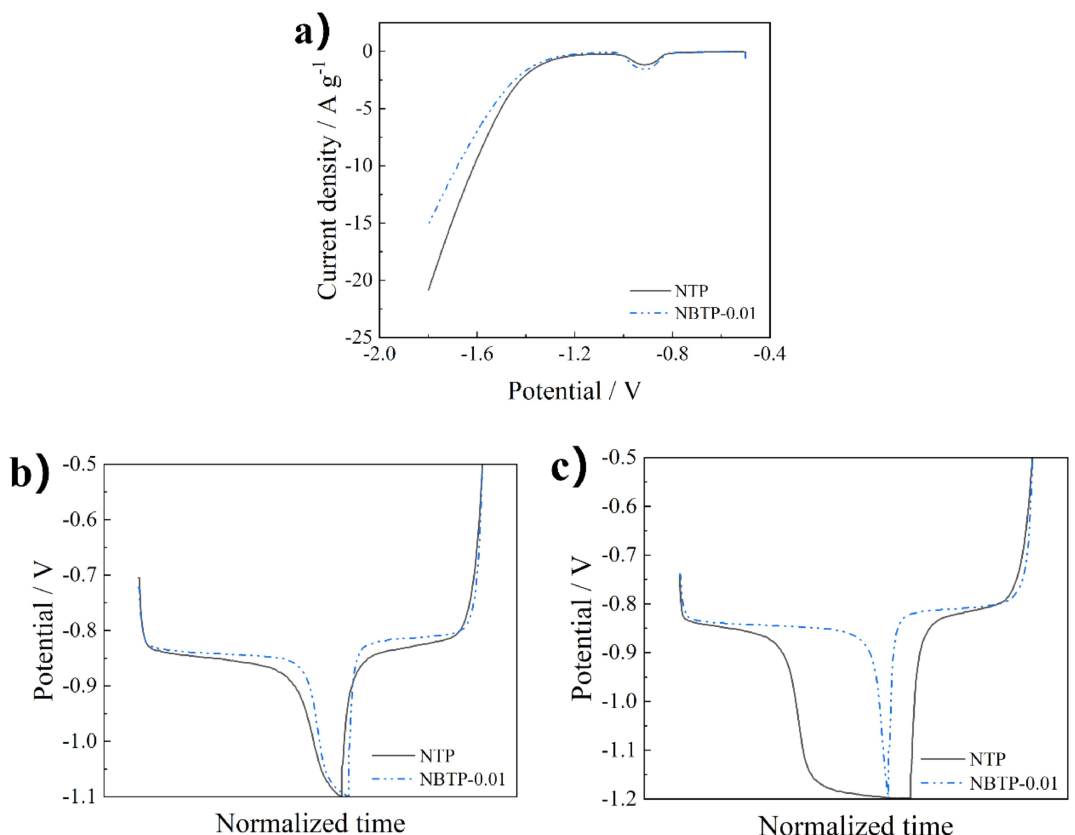


Figure 8. (a) LSV curves of NTP and NBTP-0.01; (b) charge/discharge curves with the cut-off voltage of -1.1 V; (c) charge/discharge curves with the cut-off voltage of -1.2 V.

(LSV) curves of the NTP and NBTP-0.01 anodes in 1.0 M Na₂SO₄ aqueous solution at 1.0 mVs⁻¹. It can be clearly observed from the plots of Figure 8a that the bismuth doping can shift the hydrogen evolution potential negatively and thus suppress the hydrogen evolution at the anode. In order to confirm the effect of the bismuth doping on the hydrogen evolution potential at the NTP anode, Figures 8b and c present the charge/discharge plots of the above-mentioned NTP and NBTP-0.01 half-cells with different discharge cut-off voltages. It is obvious that the possibility of the occurrence of hydrogen evolution at a discharge voltage can be estimated by the slope of the tangent lines at the end of the discharge curves in Figures 8b and c.^[42] When the discharge cut-off voltages for the corresponding half-cells are set at -1.1 V (vs. SCE), there are similar tangent slopes for the discharge plots of the NTP and NBTP-0.01 half-cells, suggesting the little possibility of the occurrence of hydrogen evolution on this condition. Then, when the discharge cut-off voltage is set at -1.2 V (vs. SCE), it can be observed that a new voltage plateau with respect to the possible hydrogen evolution reaction occurs at the end of the discharge curve of the NTP half-cell in Figure 8c, however, not observed for the NBTP-0.01 one. It reflects that the hydrogen evolution reaction at the NTP anode is easier to occur than that at the NBTP-0.01 anode, further confirming that the bismuth doping can help suppress the hydrogen evolution reaction at the anode, thereby broadening the discharge cut-off voltage and enhancing the battery capacity.

In the specific case of the hydrogen reaction mechanism, a two-step scheme has been confirmed:^[47,48] a first step consisting in the discharge of the hydrated proton (H⁺ electronation) and a following second step that could be either a recombination of the adsorbed hydrogen atoms (chemical desorption) or an ion-atom recombination known as electrochemical desorption. Either one of these steps can be rate determining, which results in the possibility of four distinct mechanisms for the hydrogen reaction. Furthermore, it has been reported that metals having more unpaired electrons in the d-band have a lower percentage of d-character, or more "holes" in the d-band, and because of the vacant orbitals in the d-band, these metals interact strongly with electron donating atoms or molecules, and hence adsorb hydrogen strongly by electron pair formation.^[49] Since the Bi element has 6 unpaired electrons in the d-band, more than 2 for the Ti element, it can be indicated that the Bi element might adsorb hydrogen more strongly by electron pair formation in contrast with the Ti element. Thus, it can be considered that the incorporation of Bi into NaTi₂(PO₄)₃ might result in the stronger adsorption (the more difficult electrochemical desorption) of the H atom on the anode surface, further suggesting the higher hydrogen evolution overpotentials at the Bi-modified NTP/C anode in this work. In fact, N. PAPAGEORGIO et al^[47] also investigated the effect of Bi content on the kinetics of the hydrogen evolution reaction at various Bi-containing Pb binary alloy electrodes, and proposed that the dominant mechanism for the hydrogen evolution reaction on Pb is changing with increasing Bi content from a rate-determining discharge followed by electrochemical desorption, to a fast discharge followed by a rate-determining electrochemical desorption in

the case of the pure Bi electrode, probably due to the stronger hydrogen adsorption on the electrode surface resulted from the addition of the Bi element. Therefore, it is further confirmed that the introduction of Bi can inhibit the occurrence of the hydrogen evolution reaction at the modified anode in this work.

Based on the above results, an anode-limited full cell system of NTP//NMO (or NBTP-0.01//NMO) was further assembled by using Na_{0.44}MnO₂ as the cathode material and 1.0 M Na₂SO₄ aqueous solution as the electrolyte. Due to its large "S" - shaped tunnel with an internal open framework structure, NMO promotes a rapid intercalation/extraction of Na⁺, making it a promising candidate material for the ASIB cathode.^[50-52] In order to achieve anode-limited capacity balance, the mass ratio of the cathode and anode active materials can be reasonably set to be about 2.4:1.0 based on their theoretical capacities, resulting in a capacity ratio of approximately 1.2:1.0.

In order to investigate the electrochemical reaction kinetics of the above-mentioned NTP and NBTP-0.01 anodes in full cells, Figure 9a illustrates the CV curves of the corresponding aqueous full cells at 0.5 mVs⁻¹. As shown in Figure 9a, both the CV curves of the two full-cells show three oxidation peaks and two reduction peaks companying with the similar intercalation/extraction processes of Na⁺. Compared with the NTP//NMO full-cell, the NBTP-0.01//NMO full-cell exhibits the higher peak current density, the larger peak area and the smaller value of ΔE_p , indicating that the NBTP-0.01//NMO one has the better electrode reaction activity, and the higher charge/discharge specific capacity. This further suggests that the NaTi₂(PO₄)₃ system doped with appropriate amounts of bismuth has the better electrochemical performance, which is consistent with the result obtained from the above-mentioned charge/discharge curves in Figures 5 and 7 for the two half-cells.

In this work, the charge/discharge capacities were estimated based on the mass of the active materials (NTP/C or Bi-doped NTP/C, with the theoretical capacity of about 133 mAh g⁻¹) of the anode. The charge/discharge plots at different C-rates for the NTP//NMO and NBTP-0.01//NMO full cells are shown in Figures 9b and c, respectively. It can be observed that there are flat charge/discharge plateaus and high reversible charge/discharge capacities for the above-mentioned two full cells, as clearly observed from the plots in Figures 9b and c. Moreover, it can be seen that the largest discharge voltage plateaus for the two cells are approximately 1.1 V (at 2 C-rate) in this work. Additionally, the corresponding overpotential of the NBTP-0.01//NMO full cell during the charge/discharge process is fairly smaller than that of the NTP//NMO one, suggesting that the Bi doping into NTP might decrease the polarization of the NTP/C anode during the electrochemical reaction process, thus enhancing the electrochemical reversibility of NTP during the charge/discharge process. The obtained results are in accord with those from the CV curves in Figure 9a. Figure 9d presents the plots of discharge capacity vs. cycle number for the NTP//NMO and NBTP-0.01//NMO full cells at 2, 5, 10, 20 C and back to 2 C rates. The NBTP-0.01//NMO full cell delivers discharge specific capacities of 94.5, 82.7, 74.5, 55.8, and 92.4 mAh g⁻¹ at 2, 5, 10, 20 C, and back to 2 C rates, respectively, which are

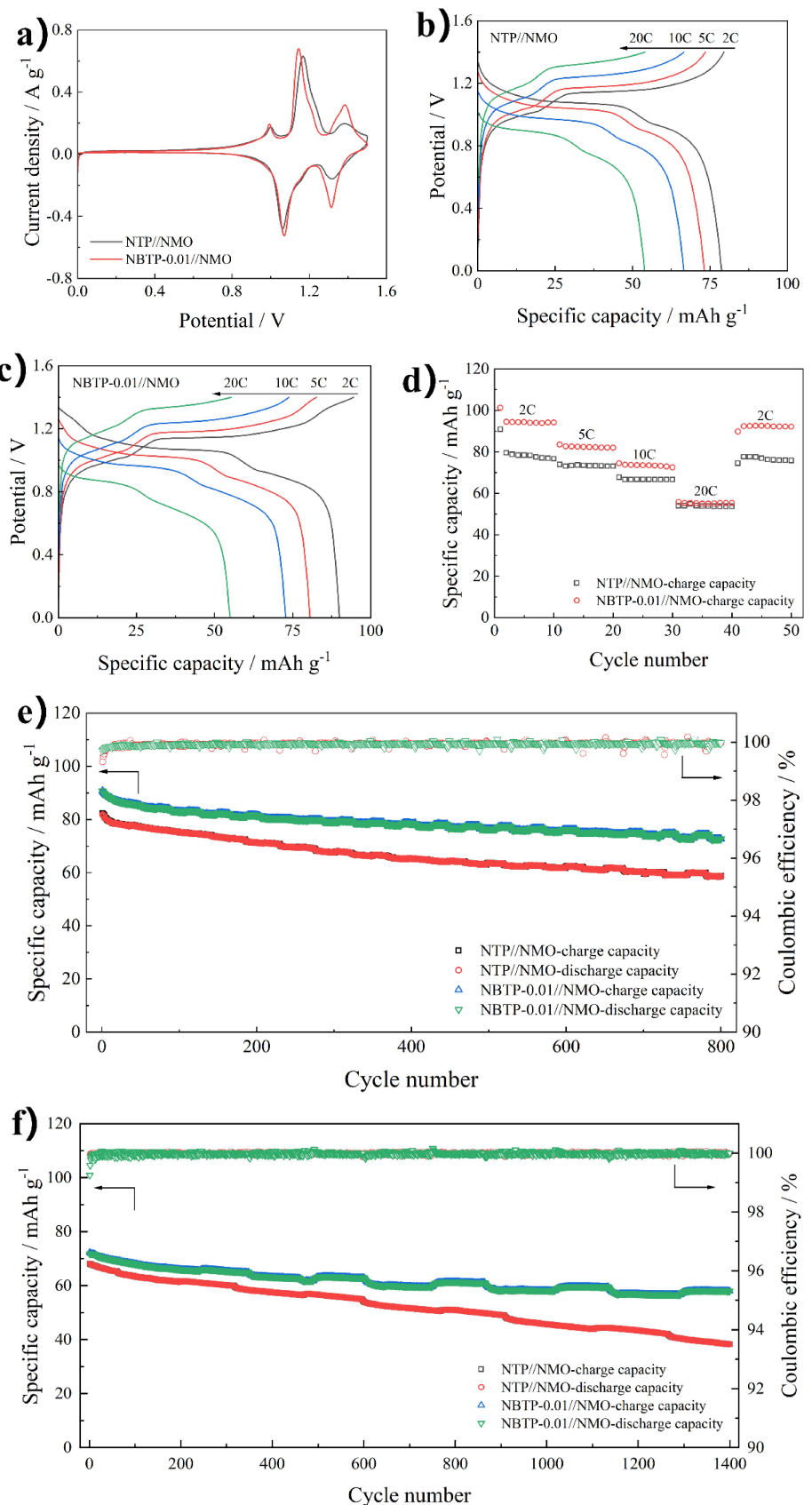


Figure 9. cyclic voltammograms (CV) (a), charge/discharge plots (b, c), rate performance at different C-rates (d), and cyclic performances at 2 C-rate (e) and 10 C-rate (f) for the NTP//NMO and NBTP-0.01//NMO full cells.

much larger than those of the NTP//NMO full cell (79.5, 73.9, 66.6, 54.0, and 77.6 mAh g⁻¹). It is indicated that the doping of the appropriate amount of bismuth into NTP can increase the discharge capacity of the full cell from 79.5 to 94.5 mAh g⁻¹ by about 18.9%. Furthermore, the NBTP-0.01//NMO full cell reaps a large capacity retention of 97.8% after the final 10 cycles at 2 C-rate, with that of 97.6% for the NTP//NMO one, indicating the excellent inherent structural stability of the corresponding anodes. The obtained results are in accord with those from the charge/discharge curves for the NBTP-0.01 half-cells in Figures 5b~c.

Figure 9e shows the plots of specific capacity and coulombic efficiency as a function of cycle number for the above-mentioned full cells at 2 C-rate for 800 cycles. It can be observed that both the full cells have a very high coulombic efficiency of around 99% during the charge/discharge processes. Additionally, the NBTP-0.01//NMO cell exhibits the better cycling performance with a larger capacity retention of about 80.1% in contrast with the NTP//NMO one (71.2%) after 800 cycles at 2 C-rate, as obtained from the plots of Figure 9e. Furthermore, the plots of specific capacity and coulombic efficiency vs. cycle number at 10 C-rate for 1400 cycles were presented in Figure 9f. It also indicates that the above-mentioned two cells show a very high coulombic efficiency of around 99%. Moreover, the NBTP-0.01//NMO cell also delivers a higher capacity retention of about 80.2% than that of the NTP//NMO one (56.2%) after 1400 cycles at 10 C-rate, as obtained from the plots of Figure 9f. Based on the above results, it is concluded that that the bismuth doping into NTP can greatly improve the cycling performance of the corresponding full cell, as similarly reported in the plots of Figure 7 for the corresponding half cells. Thereby, it is further confirmed that the introduction of bismuth ions slightly makes the cell size larger, and the possible solid BiO₆ serves as a stable and larger diffusion channel for the migration of Na⁺ within the NTP structure, thus exhibiting a longer cycle life and higher rate performance for the modified composites in contrast with the pristine one. However, it should be noted that some small regular capacity fluctuations can be observed from the plots of specific capacity vs. cycle number in Figure 9f. Since both the NMO and NTP electrodes in the NTP//NMO full cell have excellent structural stability during high-rate electrochemical reactions in water,^[53] it should be considered that the above-mentioned regular slight capacity fluctuations might be due to some unexpected changes in the environmental room temperature during the charge/discharge long-cycling processes.

In addition, due to that the electrochemical reaction processes at the electrodes of the full cells, especially the oxygen evolution reaction at the cathode and the hydrogen evolution reaction at the anode during the charge processes, can be easily affected with the change of the charge voltage, Figures 10a-c also illustrate the charge/discharge curves with varying charge cut-off voltages such as 2.1, 2.2 and 2.3 V for the above-mentioned two full cells at a 1 C-rate. It can be also obtained that the NMO cathode can be fully charged before oxygen evolution occurs in this work, as observed from the CV curves in Figure 9a when the NMO materials were used as the

working electrode during the CV tests. Thus, it can be easy to understand that the hydrogen evolution reaction at the anode is more likely to occur in comparison with the oxygen evolution reaction at the cathode for the full cells during the charging processes, as also reported by Ref [42]. That is to say, the higher charge cut-off voltage of the full cell results in the more possible occurrence of the hydrogen evolution at the anode. It can be clearly seen that there is a new plateau in the NTP//NMO full-cell charge curve at 2.3 V, not at the lower charge cut-off voltages (2.1, 2.2 V), corresponding to the hydrogen evolution at the anode that occurs at the end of the charging process. Moreover, no new plateau in the NBTP-0.01//NMO full-cell charge curves can be observed at the end of the charging processes at the charge cut-off voltages including 2.1, 2.2 or 2.3 V. Thereby, there is more evident hydrogen evolution on the charging curves of the NTP//NMO full cell in contrast with that of the NBTP-0.01//NMO one, as observed in Figures 10a-c. It suggests that the occurrence of hydrogen evolution for the NTP//NMO full-cell is indeed suppressed by the Bi doping into NTP. Furthermore, the inhibition of hydrogen evolution resulted from the Bi doping can decrease the irreversible depletion of the limited Na⁺ in the cathode material and hinder the deterioration of the charge/discharge performance of the full cell, which is of great importance for the stability of the energy storage device. In addition, the Bi doping can suppress the hydrogen evolution reaction at the anode, thereby broadening the charge cut-off voltage of the full cell and enhancing the battery capacity. Then, the discharge specific capacity and energy density for the NTP//NMO full cell with the voltage range of 0–2.2 V is 80.7 mAh g⁻¹ and 63.9 Wh kg⁻¹, respectively. Meanwhile, the corresponding values for the NBTP-0.01//NMO full cell with the voltage range of 0–2.3 V is 98.3 mAh g⁻¹ and 75.0 Wh kg⁻¹. It should be also noted that the above-mentioned charge/discharge capacities and energy densities of the aqueous anode-limited full-cells were estimated based on the mass of active materials (NTP/C or Bi-doped NTP/C, with a high theoretical capacity of about 133 mAh g⁻¹) in the anode, in an attempt to precisely illustrate the effects of the introduction of Bi on the electrochemical and charge/discharge performances of the modified anodes. It is further indicated that the expansion of the charge cut-off voltage resulted from the inhibition of the hydrogen evolution reaction can increase the discharge capacity and energy density of the modified NBTP//NMO full cell by 21.8% and 17.3% in comparison with those of the NTP//NMO one, respectively.

Based on the above results, the successful Bi doping could contribute to the inhibition of hydrogen evolution via regulation the electrode potential for hydrogen evolution at the NTP anode, also accompanying with excellent electrochemical and charge/discharge properties. The introduction of bismuth ions slightly makes the cell size larger, while the possible formed solid BiO₆ serves as a stable and larger diffusion channel for the migration of Na⁺ within the NTP structure. Consequently, the modified NBTP-0.01 composite has the highest cycle life and best rate performance in this work. Moreover, the expansion of the charge cut-off voltage resulted from the inhibition of the hydrogen evolution reaction by the Bi doping can greatly

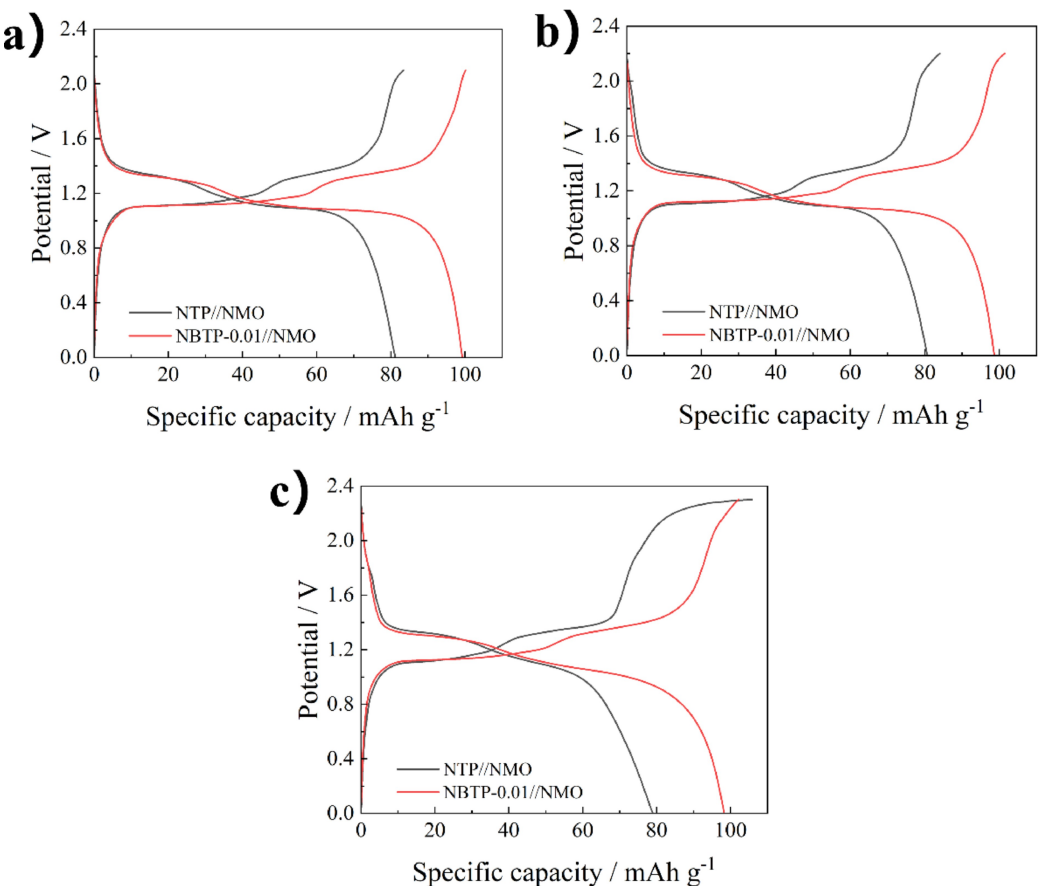


Figure 10. Charge/discharge curves for the NTP//NMO and NBTP-0.01//NMO full cells with varying charge/discharge voltage ranges:(a) 0–2.1 V; (b) 0–2.2 V; (c) 0–2.3 V.

increase the discharge capacity and energy density of the modified full cell in contrast with those of the pristine one, respectively.

3. Conclusions

A series of bismuth doped $\text{Na}_{1+x}\text{Bi}_x\text{Ti}_{2-x}(\text{PO}_4)_3/\text{C}$ ($x=0, 0.005, 0.01, 0.02$) composites were successfully synthesized by a facile sol-gel method. An appropriate proportion of Bi doping has little effect on the crystal structure of $\text{NaTi}_2(\text{PO}_4)_3$. The Bi doping can increase the lattice parameters and unit cell volume of NTP, thus contributing to the larger transport channel for Na^+ in the NTP crystal structure. The NBTP-0.01($x=0.01$) anode shows the best electrochemical performance among all the samples, might due to the larger diffusion coefficient and the effective improvement of the intrinsic ion conduction property after the appropriate amount of bismuth doping into NTP. The NBTP-0.01 anode delivers the discharge capacities of 130.0 mAh g^{-1} at 1 C-rate and 104.8 mAh g^{-1} at 2 C-rate, while The NTP anode has those of 106.5 (1 C) and 94.5 mAh g^{-1} (2 C). Moreover, the NBTP-0.01//NMO fuel cell exhibits the better cycling performance with a larger capacity retention of about 80.1% in contrast with the NTP//NMO one (71.2%) after 800 cycles at 2 C-rate. Additionally, the above-mentioned two full cells show a very

high coulombic efficiency of around 99%. Furthermore, the NBTP-0.01//NMO full cell also delivers a higher capacity retention of about 80.2% than that of the NTP//NMO one (56.2%) after 1400 cycles at 10 C-rate. The improvement of the cycling performance of the system in this work might result from the possible formed solid BiO_6 octahedra served as a stable and larger diffusion channel for the easier migration of Na^+ within the NTP structure. It was also found that bismuth doping into NTP can suppress the hydrogen evolution reaction at the anode, broaden the charge/discharge cut-off voltage, and thus enhance the battery capacity. For half-cell tests, when the discharge cut-off voltage is set at -1.2 V (vs. SCE), it can be observed that a new voltage plateau with respect to the possible hydrogen evolution reaction occurs at the end of the discharge curve of the NTP half-cell, however, not observed for the NBTP-0.01 one. It reflects that the hydrogen evolution reaction at the NTP anode is easier to occur than that at the NBTP-0.01 anode. Then, for full cell tests, it can be clearly seen that there is a new plateau in the charge curve of the NTP//NMO full-cell at 2.3 V, corresponding to the hydrogen evolution at the anode that occurs at the end of the charging process, however, not observed for the NBTP-0.01//NMO full-cell. It further suggests that the occurrence of hydrogen evolution for the NTP//NMO full-cell is indeed suppressed by the Bi doping into NTP. It is obvious that the inhibition of hydrogen evolution

resulted from the Bi doping can decrease the irreversible depletion of the limited Na^+ in the cathode material and hinder the deterioration of the charge/discharge performance of the full cell, which is of great importance for the stability of the energy storage device. The discharge specific capacity and energy density for the NBTP-0.01//NMO full cell is 98.3 mAh g^{-1} and 75.0 Wh kg^{-1} , while the corresponding values for the NTP//NMO full cell is 80.7 mAh g^{-1} and 63.9 Wh kg^{-1} , respectively. Thereby, the expansion of the charge cut-off voltage resulted from the inhibition of the hydrogen evolution reaction after the Bi doping into NTP can finally increase the discharge capacity and energy density of the modified NBTP//NMO full cell by 21.8% and 17.3%, respectively. This work of great significance to develop practical $\text{NaTi}_2(\text{PO}_4)_3/\text{C}$ anode materials, promote the stability of ASIB performance, and accelerate the commercialization of ASIB.

Acknowledgements

This work was supported by the Guangdong Basic and Applied Basic Research Foundation, China (NO. 2019A1515110825).

Conflict of Interests

There are no conflicts to declare.

Data Availability Statement

Research data are not shared.

Keywords: Aqueous Na-ion batteries • $\text{NaTi}_2(\text{PO}_4)_3$ anode • Bi doping • Cycling stability • Hydrogen evolution

- [1] Y. Wu, W. Shuang, Y. Wang, F. Chen, S. Tang, X. Wu, Z. Bai, L. Yang, J. Zhang, *Electrochim. Energy Rev.* **2024**, 7, 17.
- [2] T. Mu, Z. Wang, N. Yao, M. Zhang, M. Bai, Z. Wang, X. Wang, X. Cai, Y. Ma, *J. Energy Storage* **2023**, 69, 107917.
- [3] Z. Hou, X. Chen, J. Liu, Z. Huang, Y. Chen, M. Zhou, W. Liu, H. Zhou, *J. Power Sources* **2024**, 601, 234242.
- [4] W. Liao, T. Hung, M. Abdelaal, C. Chao, C. Fang, S. Mohamed, C. Yang, *J. Energy Storage* **2022**, 55, 105719.
- [5] W. Zheng, M. Wu, C. Yang, Z. Tang, H. Hu, *Ceram. Int.* **2020**, 46, 12921.
- [6] Z. Yang, C. Li, Z. Wu, H. Zhong, L. Tan, *Mater. Res. Appl.* **2024**, 18, 195.
- [7] S. Wu, T. Bashir, Y. Zhang, L. Gao, *J. Solid State Electr.* **2025**, 29, 61.
- [8] Y. Wang, H. Li, S. Di, B. Zhai, P. Niu, A. Kelarakis, S. Wang, L. Li, *Carbon Energy* **2024**, 6, e388.
- [9] J. Zhang, S. Ma, J. Zhang, J. Zhang, X. Wang, L. Wen, G. Tang, M. Hu, E. Wang, W. Chen, *Nano Energy* **2024**, 128, 109814.
- [10] C. Deng, Y. Li, J. Huang, *Small Methods* **2024**, 8, 2300832.
- [11] M. Maniscalco, M. Volpe, A. Messineo, *Energies* **2020**, 13, 4098.
- [12] L. Li, Q. Zhang, B. He, R. Pan, Z. Wang, M. Chen, Z. Wang, K. Yin, Y. Yao, L. Wei, L. Sun, *Adv. Mater.* **2022**, 34, 2104327.
- [13] H. Kim, J. Hong, K. Park, H. Kim, S. Kim, K. Kang, *Chem. Rev.* **2014**, 114, 11788.
- [14] C. Ding, Z. Chen, C. Cao, Y. Liu, Y. Gao, *Nano-Micro Lett.* **2023**, 15, 192.
- [15] M. Li, Z. Du, M. A. Khaleel, I. Belharouak, *Energy Storage Mater.* **2020**, 25, 520.
- [16] M. Lu, Y. Yan, Y. Zheng, W. Zhang, X. He, Z. Wu, T. Yang, X. Xia, H. Huang, Y. Xia, Y. Gan, J. Zhang, *Mater. Today Energy* **2023**, 38, 101454.
- [17] C. Delmas, *Adv. Energy Mater.* **2018**, 8, 1703137.
- [18] X. Pu, K. Yang, Z. Pan, C. Song, Y. Lai, R. Li, Z. Xu, Z. Chen, Y. Cao, *Carbon Energy* **2024**, 6, e449.
- [19] Y. Fang, J. Zhang, L. Xiao, X. Ai, Y. Cao, H. Yang, *Adv. Sci.* **2017**, 4, 1600392.
- [20] C. Masquelier, L. Croguennec, *Chem. Rev.* **2013**, 113, 6552.
- [21] T. Jin, H. Li, K. Zhu, P. Wang, P. Liu, L. Jiao, *Chem. Soc. Rev.* **2020**, 48, 2342.
- [22] S. Chen, C. Wu, L. Shen, C. Zhu, Y. Huang, K. Xi, J. Maier, Y. Yu, *Adv. Mater.* **2017**, 29, 1700431.
- [23] K. Wang, Y. Liu, Z. Ding, Y. Li, T. Lu, L. Pan, *J. Mater. Chem. A* **2019**, 7, 12126.
- [24] P. Wei, Y. Liu, Y. Su, L. Miao, Y. Huang, Y. Liu, Y. Qiu, Y. Li, X. Zhang, Y. Xu, X. Sun, C. Fang, Q. Li, J. Han, Y. Huang, *ACS Appl. Mater. Interfaces* **2018**, 11, 3116.
- [25] P. Lei, S. Li, D. Luo, Y. Huang, G. Tian, X. Xiang, *Electroanal. Chem.* **2019**, 847, 113180.
- [26] Y. Fang, L. Xiao, J. Qian, Y. Cao, X. Ai, Y. Huang, H. Yang, *Adv. Energy Mater.* **2016**, 6, 1502197.
- [27] Q. Hu, M. Yu, J. Liao, Z. Wen, C. Chen, *J. Mater. Chem. A* **2018**, 6, 2365.
- [28] T. Zhu, P. Hu, X. Wang, Z. Liu, W. Luo, K. Owusu, W. Cao, C. Shi, J. Li, L. Zhou, L. Mai, *Adv. Energy Mater.* **2019**, 9, 1803436.
- [29] J. Wu, L. Yang, H. Liu, H. Bu, W. Wang, C. Zeng, S. Zhu, *J. Appl. Electrochem.* **2022**, 52, 1563.
- [30] A. Mohamed, J. Whitacre, *Electrochim. Acta* **2017**, 235, 730.
- [31] W. Wu, S. Shabtag, J. Chang, A. Rutt, J. Whitacre, *J. Electrochem. Soc.* **2015**, 162, A803.
- [32] H. Tang, Z. Qu, Y. Yan, W. Zhang, H. Zhang, M. Zhu, O. Schmidt, *Mater. Futures* **2022**, 1, 022001.
- [33] X. Zhan, M. Shirpour, *Chem. Commun.* **2017**, 5, 204.
- [34] Z. Jiang, J. Zhu, Y. Li, Z. He, W. Meng, Y. Jiang, L. Dai, L. Wang, *Ceram. Int.* **2018**, 44, 15646.
- [35] Y. He, Y. Hua, Y. Wu, C. Chi, Y. Shi, C. Ai, *Electrochemistry* **2016**, 84, 705.
- [36] A. Mohamed, N. Sansone, B. Kuei, N. Washburn, J. Whitacre, *J. Electrochem. Soc.* **2015**, 162, A2201.
- [37] Z. Liu, Y. An, G. Pang, S. Dong, C. Xu, C. Mi, X. Zhang, *Chem. Eng. J.* **2018**, 353, 814.
- [38] W. Wang, J. Wu, C. Zeng, *Solid State Ionics* **2023**, 397, 116259.
- [39] P. Lei, K. Liu, X. Wan, D. Luo, X. Xiang, *Chem. Commun.* **2019**, 55, 509.
- [40] F. Zhang, W. Li, X. Xiang, M. Sun, *Chemi. – Eur. J.* **2017**, 23, 12944.
- [41] H. Wang, T. Zhang, C. Chen, M. Ling, Z. Lin, S. Zhang, F. Pan, C. Liang, *Nano Res.* **2018**, 11, 490.
- [42] Y. Qiu, Y. Yu, J. Xu, Y. Liu, M. Ou, S. Sun, P. Wei, Z. Deng, Y. Xu, C. Fang, Q. Li, J. Han, Y. Huang, *J. Mater. Chem. A* **2019**, 7, 24953.
- [43] S. Qiu, X. Wu, M. Wang, M. Lucero, Y. Wang, J. Wang, Z. Yang, W. Xu, Q. Wang, M. Gu, J. Wen, Y. Huang, Z. Xu, Z. Feng, *Nano Energy* **2019**, 64, 103941.
- [44] J. Wu, H. Liu, H. Bu, X. Zhang, H. Zhang, W. Wang, L. Yang, C. Zeng, S. Zhu, *J. Alloys Compd.* **2023**, 934, 167872.
- [45] G. Ma, Y. Zhao, K. Huang, Z. Ju, C. Liu, Y. Hou, Z. Xing, *Electrochim. Acta* **2016**, 222, 36.
- [46] H. Shi, Y. Chen, J. Li, L. Guo, *J. Colloid Interface Sci.* **2023**, 652, 195.
- [47] N. Papageorgiou, M. Skylas-Kazacos, *Electrochim. Acta* **1992**, 37, 269.
- [48] V. I. Kichigin, A. B. Shein, *J. Electroanal. Chem.* **2020**, 873, 114427.
- [49] M. M. Jakšić, *Electrochim. Acta* **1984**, 29, 1539.
- [50] G. Pang, P. Nie, C. Yuan, L. Shen, X. Zhang, J. Zhu, B. Ding, *Energy Technol.* **2014**, 2, 705.
- [51] M. Chae, Y. Elias, D. Aurbach, *ChemElectroChem* **2021**, 8, 798.
- [52] X. Zhou, A. Zhao, Z. Chen, Y. Cao, *Electrochim. Commun.* **2021**, 122, 106897.
- [53] Z. Li, D. Young, K. Xiang, W. C. Carter, Y. M. Chiang, *Adv. Energy Mater.* **2013**, 3, 290.

Manuscript received: December 4, 2024

Revised manuscript received: January 13, 2025

Accepted manuscript online: January 21, 2025

Version of record online: February 9, 2025